Materials Informatics Approach to Cu/Nb Nanolaminate Microstructure Correlations with Yield Strength and Electrical Conductivity

Takayuki Shiraiwa, Koki Yasuda, Fabien Briffod, Mark Jhon, Fergyanto Gunawan, Rahul Sahay, Nagarajan Raghavan, Arief S. Budiman, Manabu Enoki

Author information

- Takayuki Shiraiwa

Department of Materials Engineering, School of Engineering, The University of Tokyo

- Koki Yasuda

Department of Materials Engineering, School of Engineering, The University of Tokyo

- Fabien Briffod

Department of Materials Engineering, School of Engineering, The University of Tokyo

- Mark Jhon

Institute of High Performance Computing (IHPC), Agency for Science, Technology and Research (A*STAR)

- Fergyanto Gunawan

Industrial Engineering Department, BINUS Graduate Program - Master of Industrial Engineering, Bina Nusantara University

- Rahul Sahay

Xtreme Materials Laboratory (XML), Engineering Product Development, Singapore University of Technology and Design (SUTD)

Nano-Micro Reliability Lab (MRL), Engineering Product Development, Singapore University of Technology and Design (SUTD)

- Nagarajan Raghavan

Nano-Micro Reliability Lab (MRL), Engineering Product Development, Singapore University of Technology and Design (SUTD)

- Arief S. Budiman

Industrial Engineering Department, BINUS Graduate Program - Master of Industrial Engineering, Bina Nusantara University

Xtreme Materials Laboratory (XML), Engineering Product Development, Singapore University of Technology and Design (SUTD)

Department of Manufacturing and Mechanical Engineering and Technology (MMET), Oregon Institute of Technology

Oregon Renewable Energy Center (OREC), Oregon Institute of Technology

- Manabu Enoki

Department of Materials Engineering, School of Engineering, The University of Tokyo

Keywords: Cu/Nb, composite, finite element method, machine learning, conductivity

Abstract

Empirical formulas were derived for the interface shape, mechanical properties, and electrical characteristics of accumulative roll bonded (ARB) Cu/Nb laminated materials, based on relevant literature data. These formulas were incorporated into a forward analysis model using finite element analysis, enabling the calculation of yield stress and conductivity from the spatial distribution of Cu/Nb two phases. By randomly varying the layer thickness and interface shape in the two-phase spatial distribution and conducting repeated forward analyses, a database linking microstructural descriptors with yield stress and conductivity was created. These microstructural descriptors include volume fraction, geometric features, topological features, spatial correlation functions, and persistent homology. The significance of each microstructural descriptor on yield stress and conductivity was quantified using machine learning techniques. The results revealed that the Cu volume fraction, layer thickness, and 0th Betti number are crucial for yield stress, while for conductivity, the Cu volume fraction has the strongest influence, followed by layer thickness and layer continuity. Based on these outcomes, the Pareto front for ARB Cu/Nb laminates in the strength-conductivity space was presented.

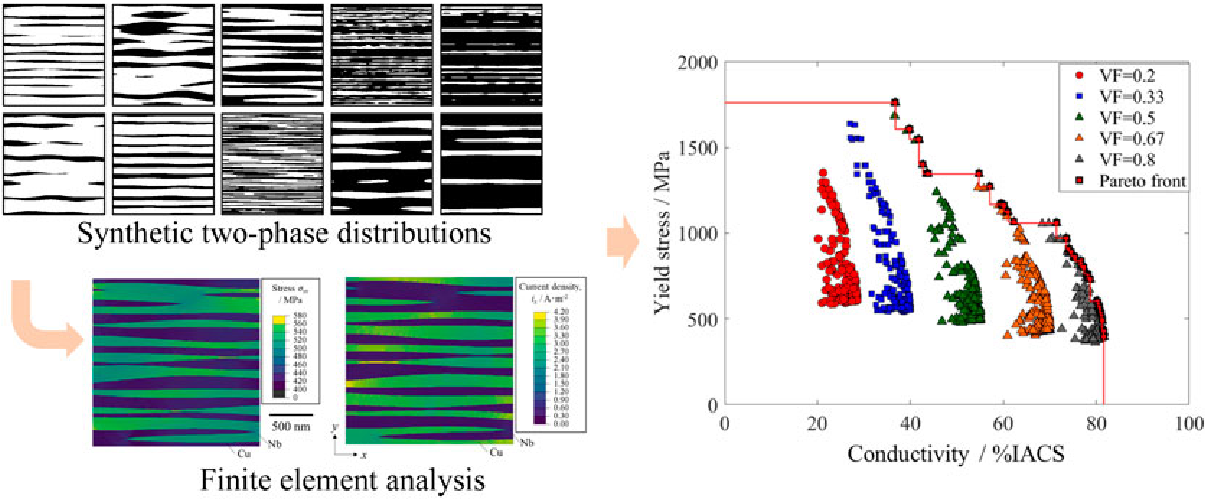

1. Introduction

High-strength, high-conductivity materials are in substantial demand across multiple fields [1]. For example, in power transmission lines and trolley wires, mechanical strength is required to withstand static loads due to self-weight, repeated loads from the environment, and friction with vehicles, while maintaining relatively high electrical conductivity. For battery connectors in electric vehicles (EVs), wiring in solar power systems, internal wiring in smartphones and tablets, and connectors linking CPUs and motherboards, materials need to withstand thermal stress and repeated loads from external vibrations. In research fields, materials capable of sustaining high Maxwell stress while maintaining conductivity are required for coils in strong magnetic field generators. Additionally, the development of high-strength, high-conductivity materials is a pivotal factor for potential and emerging applications such as electronic skin [2], flexible batteries [3], and soft robotics [4]. Traditionally, copper (Cu) alloys have been widely used for such purposes. Figure 1 illustrates the relationship between tensile strength and conductivity of major Cu alloys, distinguishing between solid-solution strengthened and precipitation-hardened types. In the figure, the IACS (international annealed copper standard) is defined by the conductivity of annealed copper, which is 5.8 × 10^7 S/m. The precipitation-hardened Cu alloys, known for their high strength, reliable fatigue resistance, and heat resistance, are used in applications such as spring materials, electrical contacts, aerospace components, and tools. This contrasts with solid-solution strengthened Cu alloys, which are favored for decorative items and plumbing materials due to their excellent workability and corrosion resistance. Precipitates in these alloys act as obstacles to dislocation movement, enhancing strength but scattering electrons and thus reducing electrical conductivity. Consequently, this introduces a trade-off, as improvements in mechanical strength often come at the expense of electrical conductivity. If both strength and conductivity could be enhanced towards the upper right direction in the figure, mechanical reliability in the various applications could be improved. This development is also expected to increase energy efficiency in these applications. It should be noted that in actual applications, other properties such as fatigue strength, fracture toughness, corrosion resistance, and bending flexibility should also be considered. Since these properties depend on the microstructure of the material, the development of high-strength, high-conductivity materials can be regarded as a multi-objective optimization problem in the structure-properties linkages.

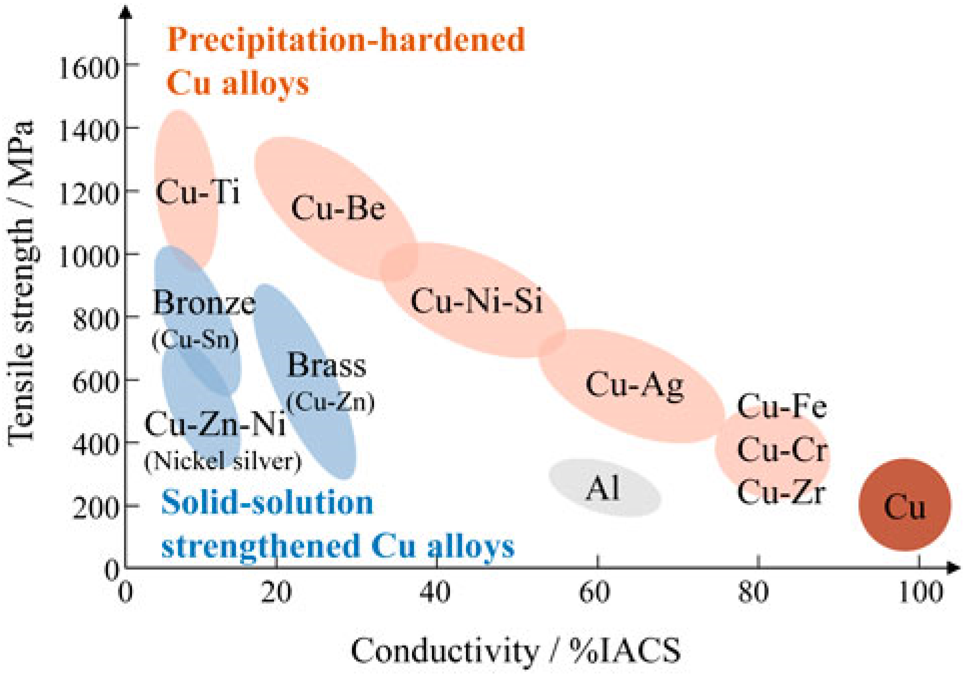

Fig. 1

Relationship between tensile strength and conductivity of major copper alloys.

To enhance multiple properties, using composite materials such as metal matrix composites (MMCs) and laminated metal composites (LMCs) is one solution. Among these, LMCs composed of high-conductivity and high-strength metals are especially promising for applications where current flows parallel to the interface. A notable example is Cu/Nb nanolaminates, which have garnered attention due to their high strength [5, 6], high conductivity [7], excellent thermal stability [8], and radiation resistance [9]. Cu/Nb nanolaminates are primarily fabricated by two methods: physical vapor deposition (PVD) and accumulative roll bonding (ARB). While PVD allows for precise control over layer thickness, it is limited in producing bulk materials, thus narrowing its application range. In contrast, ARB can produce meter-scale sheet materials through a relatively simple manufacturing process, offering broader application potential. However, ARB-produced Cu/Nb nanolaminates can exhibit variations in layer thickness, complex interface geometries, and rolling texture due to the rolling process, leading to a complex microstructure. This complexity in microstructure affects the mechanical properties and conductivity. For mechanical properties, the strength generally increases with decreasing layer thicknesses down to a few nanometers [10]. It has been reported that the interfacial sliding behavior changes due to the different interface roughness in the rolling direction (RD) and transverse direction (TD) [11, 12]. The tensile strength is found to be slightly higher in the TD compared to the RD [9], whereas ductility and fatigue life are more pronounced in the RD [13]. These differences are attributed to the texture development resulting from the rolling process and the orientation relationships at Cu/Nb interfaces. For electrical conductivity, both the layer thickness and interface roughness considerably influence conductivity [14]. The impact of phase morphology on conductivity cannot be disregarded due to its considerable significance [15]. Additionally, the rolling conditions can modify conductivity due to variations in the crystal grain size and dislocation density of each phase [16]. Thus, the structure-properties linkages in ARB Cu/Nb nanolaminates are complicated, and the relationship between microstructure and strength/conductivity needs to be quantitatively discussed using explicitly defined microstructural features.

In recent years, materials informatics (MI) has gained attention as an approach to analyze the complex and nonlinear relationship between the microstructure and properties of materials. This involves using data-driven approaches such as machine learning and Bayesian inference to interpret the connections between structure and properties. It is recognized a fundamental methodology within the frameworks of Integrated Computational Materials Engineering (ICME) [17] and Materials Integration (MInt) [18]. Since experimental data is often limited in the field of materials science, it is common to enrich the dataset using numerical methods such as first-principles calculations, molecular dynamics, and crystal plasticity finite element method (CPFEM), before employing the MI approach. However, to the best of the authors' knowledge, the application of the MI approach to Cu/Nb composites has been limited.

Therefore, this study aimed to elucidate the effects of microstructure on the mechanical properties and conductivity of ARB Cu/Nb nanolaminates through the application of a MI approach. Experimental data regarding the microstructure, conductivity, and yield stress of ARB Cu/Nb nanolaminates were gathered from the literature. Given the scarcity of experimental data, a simplified finite element analysis (FEA) was conducted to enrich the dataset on mechanical strength and conductivity. This paper focuses on extracting effective microstructural descriptors and evaluating the applicability of the MI approach. Consequently, complex models based on physical phenomena were not explored in the FEA. Instead, simple phenomenological models were utilized. The analysis emphasized the morphology of the Cu/Nb two-phases that contribute most to the properties, while the effects of grain boundaries, crystal orientation, and texture were not considered. Subsequently, machine learning methods were applied to this comprehensive dataset obtained from the FEA to investigate the correlations between microstructural descriptors and both mechanical properties and conductivity.

2. Numerical Methods

The numerical analysis for calculating the yield stress and conductivity of ARB Cu/Nb laminates was conducted in four steps: generating the two-phase spatial distribution (hereafter referred to as a "phase map"), extracting microstructural descriptors from the phase map, assigning material properties to each element, and performing FEA.

2.1 Synthetic phase map

The generation of synthetic phase map was based on literature data. Due to significant differences in interface shapes between ARB and PVD fabricated Cu/Nb laminates, this study selectively reviewed experimental data from existing literature focusing on ARB-produced laminates. It was noted that the waviness of interfaces and mechanical properties vary between the RD and TD. For the analysis of microstructure, data from the RD-ND (normal direction) plane were utilized. The microstructural analysis mainly focused on the interface morphology, which plays a characteristic role in the Cu/Nb laminates. Carpenter *et al.* produced Cu/Nb laminates with various layer thicknesses by altering the number of rolling processes, and they quantified the layer thickness variations by examining cross-sections using a scanning electron microscope (SEM) and a transmission electron microscope (TEM) [19]. In the present study, based on their experimental data, an empirical formula was derived that correlates the layer thickness ($\bar{t}_{Cu}$, $\bar{t}_{Nb}$) and its standard deviation (s_{Cu}, s_{Nb}) for each phase of Cu and Nb.

$$s_{Cu}=0.455\times\bar{t}_{Cu}^{0.721} \tag{1}$$

$$s_{Nb}=0.737\times\bar{t}_{Nb}^{0.613} \tag{2}$$

Figure 2 presents the log-log plot of the experimental data and empirical formula. The correlation coefficients were 0.978 and 0.966, respectively, demonstrating that these empirical formulae successfully reproduced the variation in layer thickness.

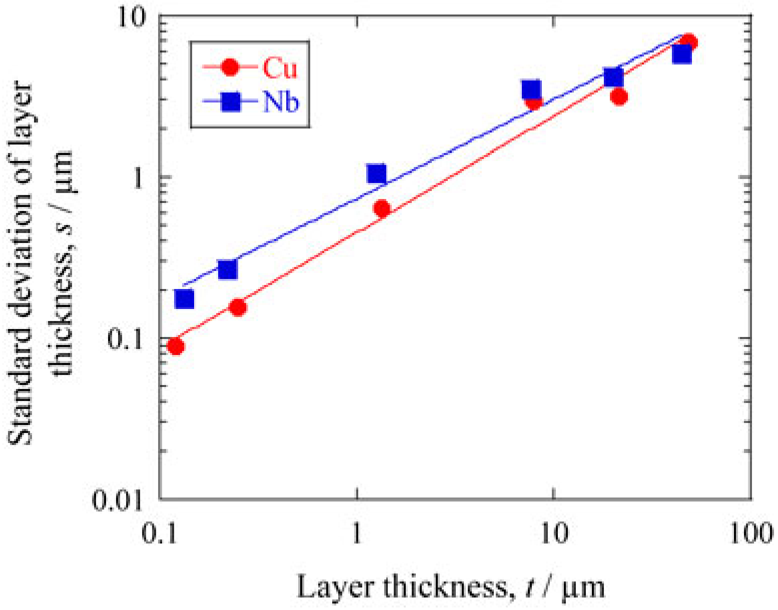

Fig. 2
Relationship between layer thickness and its standard deviation of ARB Cu/Nb laminates. Experimental data was taken from the literature [19].

Based on these validated empirical formulae, the phase map and corresponding mesh model were generated for use in the FEA. This was achieved using a procedure developed in previous studies [13]. This procedure involved creating a binary image representing each phase as 0 (Cu) and 1 (Nb). Due to significant variations in layer thicknesses from the micrometer to the nanometer scale, employing a constant size of representative volume element (RVE) would lead to an excessively large number of elements. To save computational resources, different RVE sizes were utilized for each layer thickness condition. An example of the generated phase map is presented in Fig. 3(a). The procedure for creating a phase map is outlined as follows:

1. 1. The volume fraction VF_{Cu} and mean layer thickness $\bar{t}_{Cu}$ of the Cu phase are specified. The mean layer thickness of Nb, $\bar{t}_{Nb}$, is defined as $\bar{t}_{Nb}=\bar{t}_{Cu}(1-VF_{Cu})/VF_{Cu}$.
2. 2. The standard deviations of layer thickness for each phase, s_{Cu} and s_{Nb}, are determined based on eqs. (1)–(2).
3. 3. The dimensions of two-dimensional (2D) RVE are determined to include a minimum of

10 layers.

4. 4. The construction of the two-phase spacial distribution starts from the origin of the RVE.
5. 5. Move in the y-direction by the thickness of one layer. The thickness of the layer is determined by sampling from a normal distribution with mean t_{Cu} and standard deviation s_{Cu}.
6. 6. Draw a sine wave of s_{cu} $\sin(2\pi x/\lambda + \phi)$ in the x-direction, where λ is sampled randomly from a uniform distribution in the range of 1/10 to 1 times the RVE size, and ϕ is sampled randomly within the range of $-\pi$ to π. The area below the sine wave is assigned as the Cu phase.
7. 7. Determine the thickness of the next Nb layer by sampling from a normal distribution with mean t_{Nb} and standard deviation s_{Nb}, and move in the y-direction by this layer thickness. Draw a sine wave as in step 6. Assign the Nb phase to the unassigned areas beneath the sine wave.
8. 8. Repeat steps 5–7 until the y-coordinate exceeds the y-dimension of the RVE.
9. 9. Finally, smooth the entire RVE with a 2D Gaussian smoothing kernel. The standard deviation of the kernel is set to half the average of t¯Cut¯Cu and t¯Nbt¯Nb.

The phase map created using this procedure is presented together with the experimental phase map in Fig. 3(a) and (b). The Cu volume fraction and layer thicknesses used in creating the phase maps are consistent with the experimental data. Although there are slight variations in the finer details, the overall geometrical shapes are successfully reproduced. Furthermore, Fourier transform analysis of each image is depicted in Fig. 3(c) and (d), confirming that they exhibit similar distributions in the frequency space.

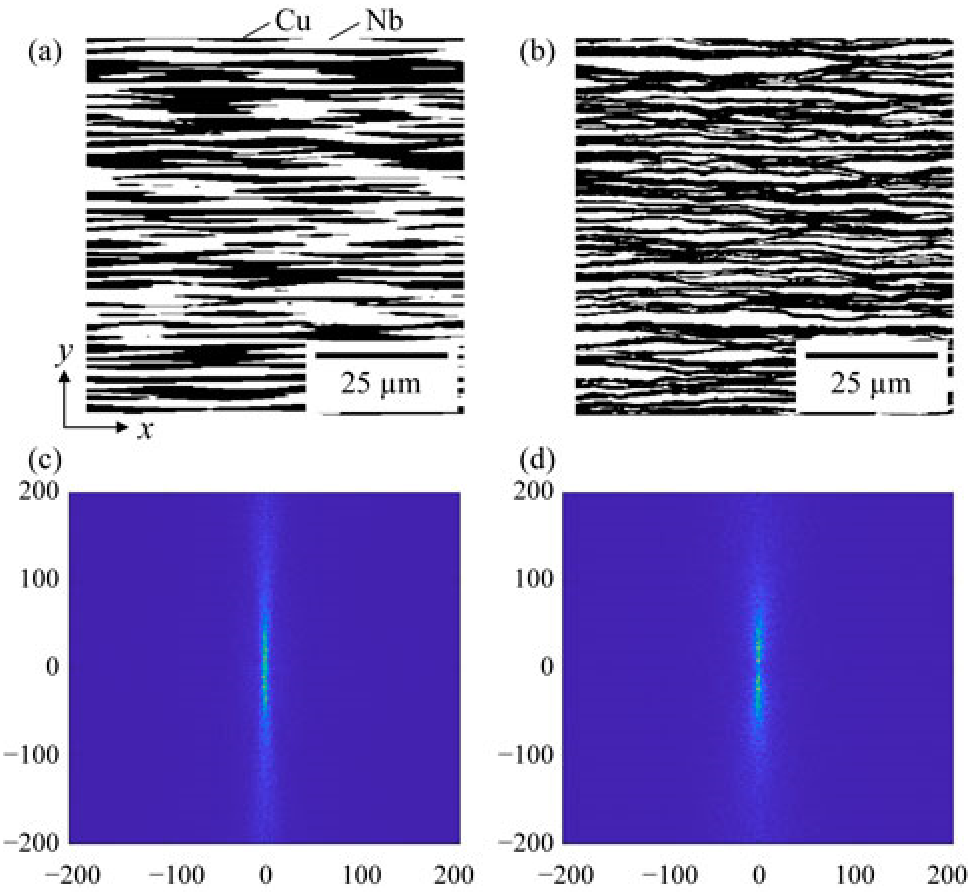

Fig. 3

(a) Synthetic phase map, (b) experimental phase map (VF_{Cu} = 0.5, t_{Cu} = 500 nm), (c) and (d) frequency domain representation of (a) and (b), respectively. The experimental phase map was obtained by binarizing a SEM image from literature [19].

2.2 Microstructural descriptors

To facilitate machine learning, a database of phase maps was created by repeating the previously described procedure. The volume fraction of the Cu phase, VF_{Cu}, was varied to 0.20, 0.33, 0.50, 0.67, and 0.80. The mean layer thickness of the Cu phase was randomly sampled from a logarithmic uniform distribution ranging from 5 nm to 20 μm. For each VF_{Cu}, 200 phase maps were created, resulting in a total of 1000 phase maps. Examples of these phase maps are shown in Fig. 4. The RVE size is different for each model. The volume fraction of VF_{Cu} = 0.50 corresponds to the materials used in the studies by Nizolek *et al.* [8] and Carpenter *et al.* [19] and in the authors' previous experiments [13]. The volume fraction of VF_{Cu} = 0.67 corresponds to the experimental studies by Ding *et al.* [7] To analyze the relationship between microstructure and properties, microstructural descriptors were extracted from the phase maps. The extracted descriptors are listed in Table 1. As geometric descriptors, in addition to the volume fraction of the Cu phase, the minimum layer thickness, $t_{min} = \min(\bar{t}_{Cu}, \bar{t}_{Nb})$, minimum curvature of the Cu/Nb interface, average size of isolated Cu phases, perimeter and circularity of isolated Cu phases were extracted. A covariogram [20, 21] was also calculated to quantify the intensity of the band structure along the loading direction. As topological descriptors, layer continuity [9], the 0th and 1st Betti numbers, and Euler characteristics were computed. Spatial correlation (SC) [22, 23], and persistent homology (PH) [24] were also calculated. The Betti numbers are defined as the rank of the *n*-th homology group. Intuitively, the 0th and 1st Betti numbers correspond to the number of *n*-dimensional connected components and the number of *n*-dimensional holes, respectively. Here, an *n*-dimensional connected component refers to a self-contained part not enclosed by an *n*-1 dimensional boundary, while an *n*-dimensional hole refers to a region enclosed by an *n*-1 dimensional boundary. In this study, considering 2D binary images and focusing on the Cu phase, the 0th Betti number corresponds to the number of connected Cu phases. Similarly, the 1st Betti number corresponds to the number of holes in the Cu phase, which equivalently refers to the number of connected Nb phases. The SC represents the relative position of the two phases, while the PH can quantify the connectivity of the phases, both of which are increasingly gaining attention in recent materials science. The persistence diagrams (PD) was computed by HomCloud [25]. Principal component analysis (PCA) was applied to SC and PH for dimensionality reduction. The calculation methods for descriptors other than layer continuity are documented in the literature [26, 27]. The layer continuity is defined by the following equation as the length of continuous Cu layers divided by the total length of Cu layers [9].

$$cont = \frac{\sum l_{cont}}{\sum l_{cont} + \sum l_{discont}} \quad (3)$$

where l_{cont} and $l_{discont}$ are the lengths of the continuous and discontinuous layers in the current loading direction (*x*-axis direction), respectively. In calculating l_{cont} and $l_{discont}$, the *x*-coordinates of the left and right edges of each isolated Cu layer were identified. Layers with edges aligning with the RVE's left and right boundaries are included in l_{cont}, while those not aligning are accounted for in $l_{discont}$. The calculation of l_{cont} and $l_{discont}$ were performed automatically through computer algorithms.

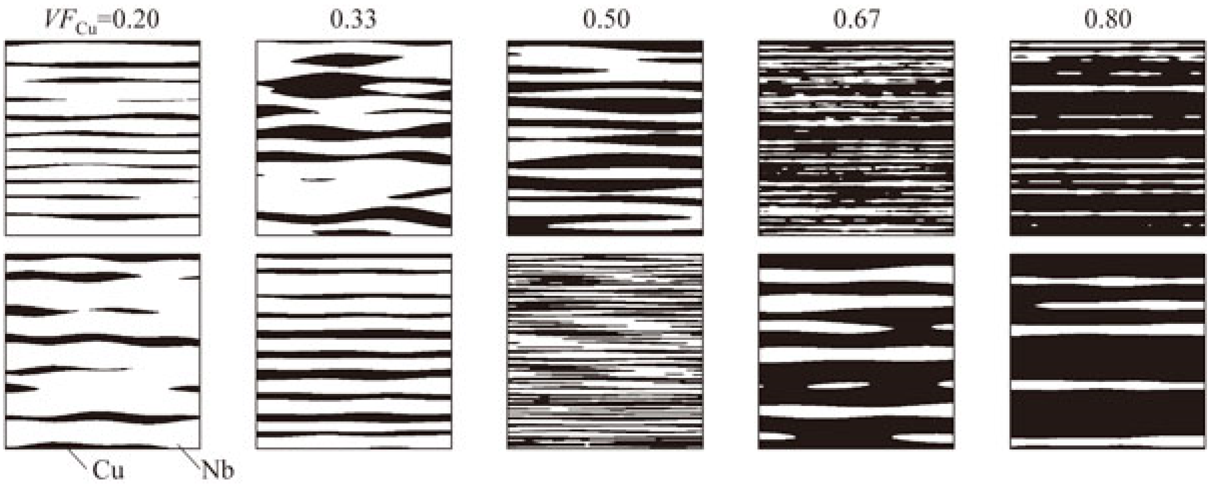

Fig. 4

Examples of synthetic phase maps with VF_{Cu} = 0.20, 0.33, 0.50, 0.67, 0.80.

Table 1 Nomenclature of microstructural descriptors and their range in the database of 1000 phase maps.

Classification	Symbol	Description	Minimum	Maximum	Mean	Variance
Geometric descriptors	VF_{Cu}	Volume fraction of Cu phase	0.20	0.80	0.50	0.05
	t_{min}	Minimum layer thickness of Cu or Nb phase, min(t_{Cu}, t_{Nb}) (unit: nm)	5	19927	2529	1.84×10^{7}
	cur	Minimum value of local curvatures of Cu/Nb interfaces (unit: nm)	0.2	2345	485	5.92×10^{5}
	$\sqrt{area}$	Average of the square root of the area of isolated Cu regions (unit: nm)	43.2	3.57×10^{5}	3.46×10^{4}	4.02×10^{9}
	$perim$	Average of perimeter of isolated Cu regions (unit: nm)	379.2	4.56×10^{6}	3.07×10^{5}	4.02×10^{11}
	cir	Average of circularity of isolated Cu regions	0.03	0.67	0.23	0.01
Topological descriptors	$cont$	Layer continuity	0	1.00	0.81	0.07
	b_0	0th Betti number of Cu phase (equivalent to the number of isolated Cu regions)	1	79	8.82	98.1
	b_1	1st Betti number of Cu phase (equivalent to the number of isolated Nb regions)	1	79	9.93	119.2
	χ	Euler characteristic of Cu phase, $\chi = b_0 - b_1$	-72	73	-1.11	162.8
Covariogram	HM	Position of the first maximum peak of the covariogram (unit: nm)	1	111	25.8	340.0
	BI	Difference between the first maximum and minimum of the covariogram	0	0.27	0.07	0.00
Spatial correlation	SC_2	2nd principal component of autocorrelation of Cu phase	-8.45	26.88	0.00	38.61
	SC_3	3rd principal component of autocorrelation of Cu phase	-33.59	18.83	0.00	29.95
	SC_4	4th principal component of autocorrelation of Cu phase	-31.17	36.55	-0.01	25.79
	SC_5	5th principal component of autocorrelation of Cu phase	-20.94	26.62	0.00	22.52
	SC_6	6th principal component of autocorrelation of Cu phase	-14.33	24.13	0.00	18.20
Persistent homology	PH_1	1st principal component of 0th persistence diagram of Cu phase	-8.34	113.5	0.01	208.8
	PH_2	2nd principal component of 0th persistence diagram of Cu phase	-75.25	34.38	0.00	72.41
	PH_3	3rd principal component of 0th persistence diagram of Cu phase	-38.75	47.98	0.00	32.22
	PH_4	4th principal component of 0th persistence diagram of Cu phase	-32.90	19.95	0.00	14.35
	PH_5	5th principal component of 0th persistence diagram of Cu phase	-19.59	40.82	0.00	9.60
	PH_6	6th principal component of 0th persistence diagram of Cu phase	-24.35	29.69	0.00	9.22

2.3 Assignment of material properties

For the mechanical properties, Nizolek *et al.* conducted tensile tests in both the RD and TD directions, revealing a Hall-Petch type relationship between layer thickness and yield stress [8]. This phenomenon is attributed to the role of interfaces as obstacles to dislocation movement. TEM observations have revealed that at layer thicknesses of several tens of nanometers, confined layer slip (CLS) becomes the dominant deformation mechanism [28]. Furthermore, Subedi *et al.* showed that a Hall-Petch type formula more accurately represents the experimental strength data of various metallic multilayer materials when compared to other models, such as the CLS model [10, 29]. Their findings imply that the Hall-Petch type relationship is valid for layer thicknesses down to 5 nm. Therefore, in the forward analysis described in the subsequent section, it was assumed that the yield stress of each phase follows a Hall-Petch type relationship with layer thickness.

Ding *et al.* investigated the relationship between layer thickness and electrical resistivity of ARB Cu/Nb laminates [7]. While electron scattering due to phonons, interfaces, grain boundaries, dislocations, and impurities can affect electrical resistance, by combining various theoretical formulas and fitting them to experimental data of resistivity, it was found that only phonon and interface scattering have significant effects on electrical resistance. The contribution of phonon scattering is represented as follows:

$$\rho^{Cu}_{pho} = \alpha_{Cu} T + b_{Cu}, \tag{4}$$

$$\rho^{Nb}_{pho} = \alpha_{Nb} T + b_{Nb}, \tag{5}$$

where T is absolute temperature, α_{Cu} and α_{Nb} are temperature-dependent coefficients, and b_{Cu} and b_{Nb} are constants. Using a temperature T = 300 K and values from the literature (α_{Cu} = 0.0072, α_{Nb} = 0.062, b_{Cu} = −0.424, b_{Nb} = −2.747) [30], the resistivities are found to be $\rho^{Cu}_{pho} = 1.736$ μΩ·cm and $\rho^{Nb}_{pho} = 15.85$ μΩ·cm, respectively. The contribution of interface scattering can be expressed by the following equations:

$$\rho^{Cu}_{int} = \frac{3}{4}\left(3\pi^2\right)^{\frac{1}{3}} \frac{\hbar}{e^2} (1-p) \frac{1}{t_{Cu}} n_{Cu}^{-\frac{2}{3}}, \tag{6}$$

$$\rho^{Nb}_{int} = \frac{3}{8}\left(3\pi^2\right)^{\frac{1}{3}} \frac{\hbar}{e^2} (1-p) \frac{1}{t_{Nb}} n_{Nb}^{-\frac{2}{3}}, \tag{7}$$

where e is the elementary charge (1.602 × 10^{-19} C), $\hbar$ is the reduced Planck constant (1.055 × 10^{-34} J·s), p is the elastic scattering probability at interfaces, t_{Cu} and t_{Nb} are the layer thicknesses of the Cu and Nb phases respectively, and n_{Cu} and n_{Nb} are the free electron densities of the Cu and Nb phases respectively (n_{Cu} = 8.45 × 10^{28} m^{-3}, n_{Nb} = 5.56 × 10^{28} m^{-3}). However, in their studies, the value of the elastic scattering probability p was not derived. In the current study, the p value was determined by fitting it to the experimental resistivity data presented in the paper using eqs. (5)–(6), under the assumption that contributions other than phonon and interface scattering can be ignored, i.e. $\rho^{Cu} = \rho^{Cu}_{int} + \rho^{Cu}_{pho}$ and $\rho^{Nb} = \rho^{Nb}_{int} + \rho^{Nb}_{pho}$. As shown in Fig. 5, equations with p = 0.90 provided a good agreement with the experimental data. This suggests that scattering at the Cu/Nb interface is close to perfect specular scattering, contrasting with heavily drawn Cu-Nb alloys where the p value is close to 0, i.e. complete diffuse scattering [31]. In the FEA, the resistivity calculated from these empirical formulas was assigned to each element.

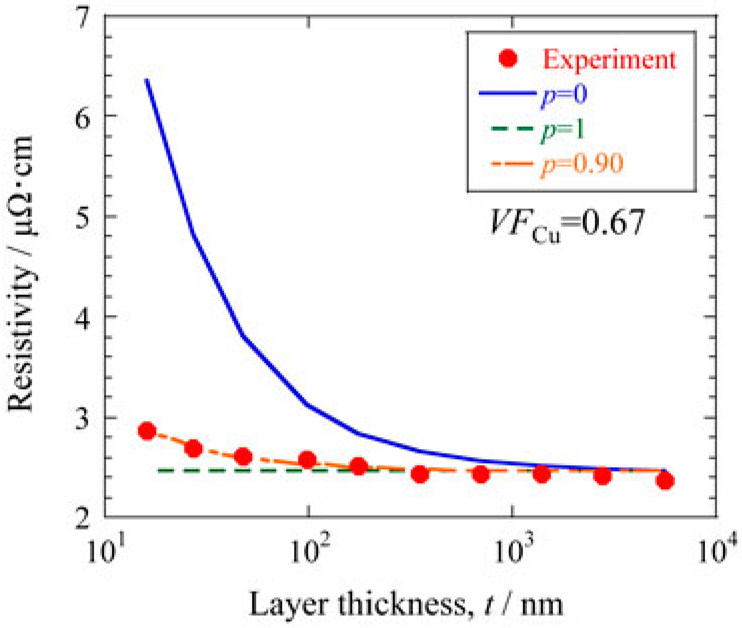

Fig. 5

Relationship between layer thickness and resistivity. Experimental data was taken from the literature [7].

2.4 Finite element analysis (FEA)

The phase maps were meshed using four-node elements, with a total element count of 160,000. For the analysis of tensile properties, plane strain elements were utilized, and loading was applied along the *x*-axis direction, as shown in Fig. 6(a). Constraints were added to ensure that the displacements of X0 and X1, Y0 and Y1, were linked to maintain flat edges. Since the Cu/Nb interface is a semi-coherent interface with high interfacial strength, this simulation assumed complete adhesion and bonding for the interface. The material constants were calibrated to align with the macroscopic yield stress (0.2% proof stress) observed in the RD direction, as investigated by Nizolek *et al.* [8] This calibration utilized phase maps with a Cu volume fraction of VF_{Cu} = 0.50 and layer thicknesses of 30 nm, 65 nm, 140 nm, 245 nm, 500 nm, 1800 nm. The calibrated material constants for each phase are presented in Table 2.

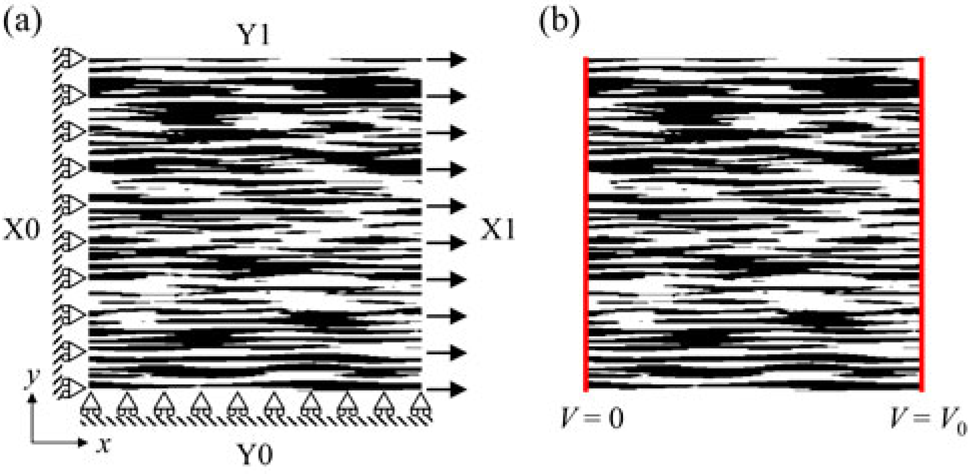

Fig. 6

Boundary conditions of (a) tensile simulation and (b) electrical conductivity simulation.

Table 2 Mechanical properties of each phase.

	Young's modulus / GPa	Poisson's ratio	Yield stress, σ_{y0} / MPa	Strain hardening exponent	Hall-Petch coefficient / $MPa \cdot nm^{1/2}$
Cu	130	0.33	250	0.3	2000
Nb	103	0.33	450	0.2	

FEA is also useful for calculating the effective electrical conductivity of composite materials, taking into account their microstructures, as highlighted in references [32, 33]. For the above mesh models, resistivity defined by eqs. (3) to (6) was assigned to each element. The current density distribution within the RVE was calculated using the FEM software Abaqus by applying a constant voltage to the left and right boundaries of the RVE, as shown in Fig. 6(b). The governing equation for the electric field is derived from Maxwell's equations, representing the conservation of charge, and the current flow is described by Ohm's law. By integrating the current density at the left boundary (X0), the total current was calculated. The effective electrical resistance of the RVE was obtained by dividing the applied voltage by the total current flowing through it. The resistivity was then deduced by multiplying the obtained resistance by the RVE's cross-sectional area and dividing it by its length. Finally, conductivity was determined as the reciprocal of the resistivity.

3. Results

3.1 Yield stress and conductivity obtained by FEA

As an example of the FEA results, the stress distribution for a volume fraction VF_{Cu} = 0.50 is shown in Fig. 7(a). From the stress distribution, it is evident that the Nb phase supports more external load than the Cu phase. Within the Nb phase, the stress is not uniform and tends to concentrate in the thinner, constricted regions. Thus, it can be inferred that the deformation behavior of the entire Cu/Nb laminate depends not only on the volume fraction of the Nb phase but also on its spatial distribution. The corresponding stress-strain curves are presented in Fig. 7(b). For yield stress determination, the stress values were divided by an average elastic modulus of 116.5 GPa to represent the elastic strain. The macroscopic plastic strain was calculated by subtracting the elastic strain from the total strain. The yield stress was then defined as the stress level at 0.2% of the calculated macroscopic plastic strain.

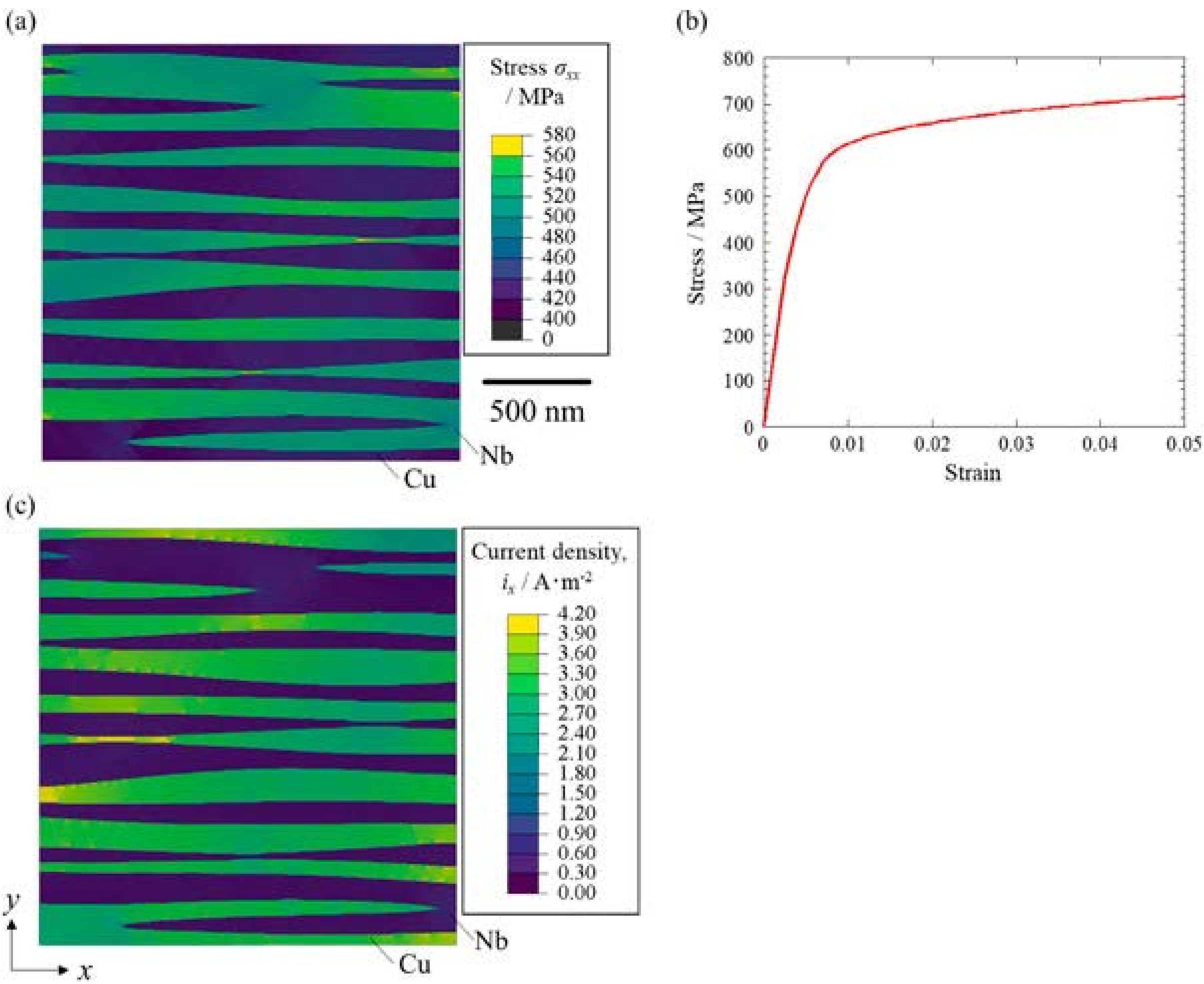

Fig. 7

(a) Stress distribution after yielding, (b) stress-strain curve, and (c) distribution of current density in x direction. The selected phase map corresponds to the central image in the top row of Fig. 4, characterized by VF_{Cu} = 0.50 and t_{Cu} = 224 nm.

The current density distribution for the same phase map is shown in Fig. 7(c). Since the Cu phase is approximately nine times more conductive than the Nb phase, most of the current flows through the Cu phase. Focusing on the Cu phase, layers that are continuously connected from the left to the right edge of the model exhibit higher current density compared to those with interruptions along the way. Furthermore, Cu regions with narrower widths tend to have higher current density, while areas where two Cu layers are close together exhibit reduced current density due to possible electrical conduction through the Nb phase. Consequently, it can be inferred that the electrical properties of the entire RVE strongly depend on the spatial distribution of the Cu phase.

The calculated yield stress and electrical conductivity for the 1000 phase maps are presented in Fig. 8(a) and (b), respectively. It can be seen that the yield stress strongly depends on the layer thickness. This is attributed to the incorporation of the Hall-Petch effect for layer thickness in defining material properties. When the layer thickness is large, the yield stress increases with the volume fraction of the Nb phase. Conversely, for small layer thicknesses (around 5 nm), the yield stress reached a maximum at VF_{Cu} = 0.5. This is because the Hall-Petch effect is maximized in both phases at this condition. For comparison, the experimental results at VF_{Cu} = 0.5 are plotted as squares within the figure. The FEA effectively reproduces the experimental results for yield stress across various layer thicknesses.

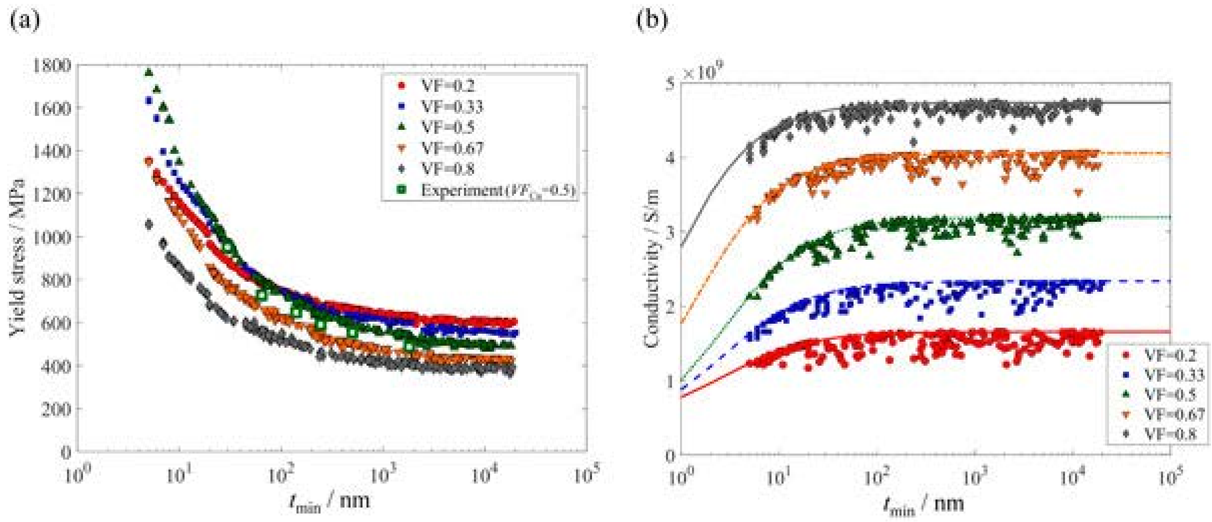

Fig. 8
Calculation results of (a) yield stress and (b) conductivity for the synthetic phase map database. The horizontal axis is the minimum layer thickness of the Cu or Nb phase. Experimental data of yield stress (VF_{Cu} = 0.5) was taken from literature [6].

The electrical conductivity also exhibits a strong dependence on both VF_{Cu} and layer thickness, as shown in Fig. 8(b). The curves in the figure represent theoretical values assuming a parallel circuit in the *x*-axis direction for each volume fraction and were calculated using the following equation.

$$\frac{1}{\rho}=\frac{V_{Cu}}{\rho_{Cu}}+\frac{1-V_{Cu}}{\rho_{Nb}} \quad (8)$$

where ρ represents the resistivity of the RVE, which is the reciprocal of conductivity. The results obtained through FEM calculations generally agreed with the theoretical values but were slightly lower due to the roughness of the interfaces. In comparison to the yield stress results, a larger scatter was observed, suggesting that conductivity is more susceptible to the interface geometry than yield stress.

3.2 Importance analysis

To identify important microstructural descriptors for each property, importance analysis using random forest (RF) regression was conducted. The inputs for RF regression were microstructural descriptors of 1000 phase maps (Table 1), and the output was the yield stress or electrical conductivity obtained through FEM. The RF is an ensemble machine learning method that constructs multiple regression trees as weak learners, and the regression trees were built based on the method using chi-squared analysis [34]. The importance of descriptors was quantified using the mutation-based mean squared reduction method [35]. The importance corresponds to the average change in the mean squared error of predictions when out-of-bag data (data not used in training) are permuted for each decision tree.

The results of the importance analysis for yield stress are shown in Fig. 9(a). It was observed that VF_{Cu} had the highest importance, which is consistent with the fact that as VF_{Cu} increases, the amount of Nb phase supporting the external load decreases, resulting in a decrease in yield stress. Following VF_{Cu}, the importance was relatively high for the 0th Betti number (b_0), layer thickness (t_{min}), and the average size of the Cu phase ($\sqrt{area}$). The importance analysis for electrical conductivity is presented in Fig. 9(b). Notably, VF_{Cu} had significantly higher importance compared to other descriptors. This can be attributed to the approximately nine-fold difference in conductivity between the two phases, making the influence of Cu volume fraction particularly pronounced in comparison to yield stress. Additionally, layer thickness (t_{min}) and layer continuity (*cont*) showed relatively high importance in influencing electrical conductivity.

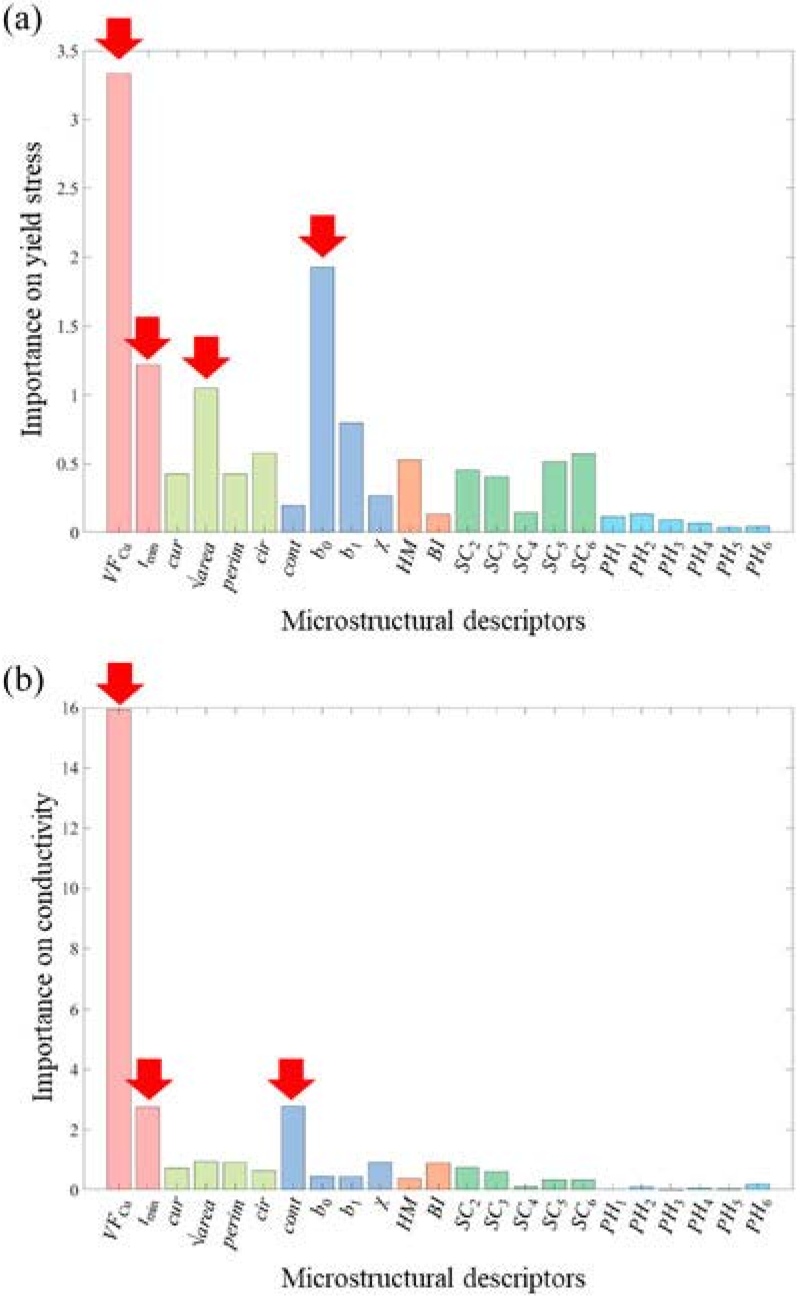

Fig. 9

Results of importance analysis by random forest regression. Importance on (a) yield stress and (b) conductivity.

The results of correlation analysis to examine the relationships between important descriptors are shown in Fig. 10. It was observed that there is a strong correlation only between t_{min} and √area√area. Given that t_{min} has a more clear physical interpretation, √area√area was excluded from further consideration. Therefore, for yield stress, the important descriptors are VF_{Cu}, t_{min}, and b_0, while for electrical conductivity, the important descriptors are VF_{Cu}, t_{min}, and *cont*.

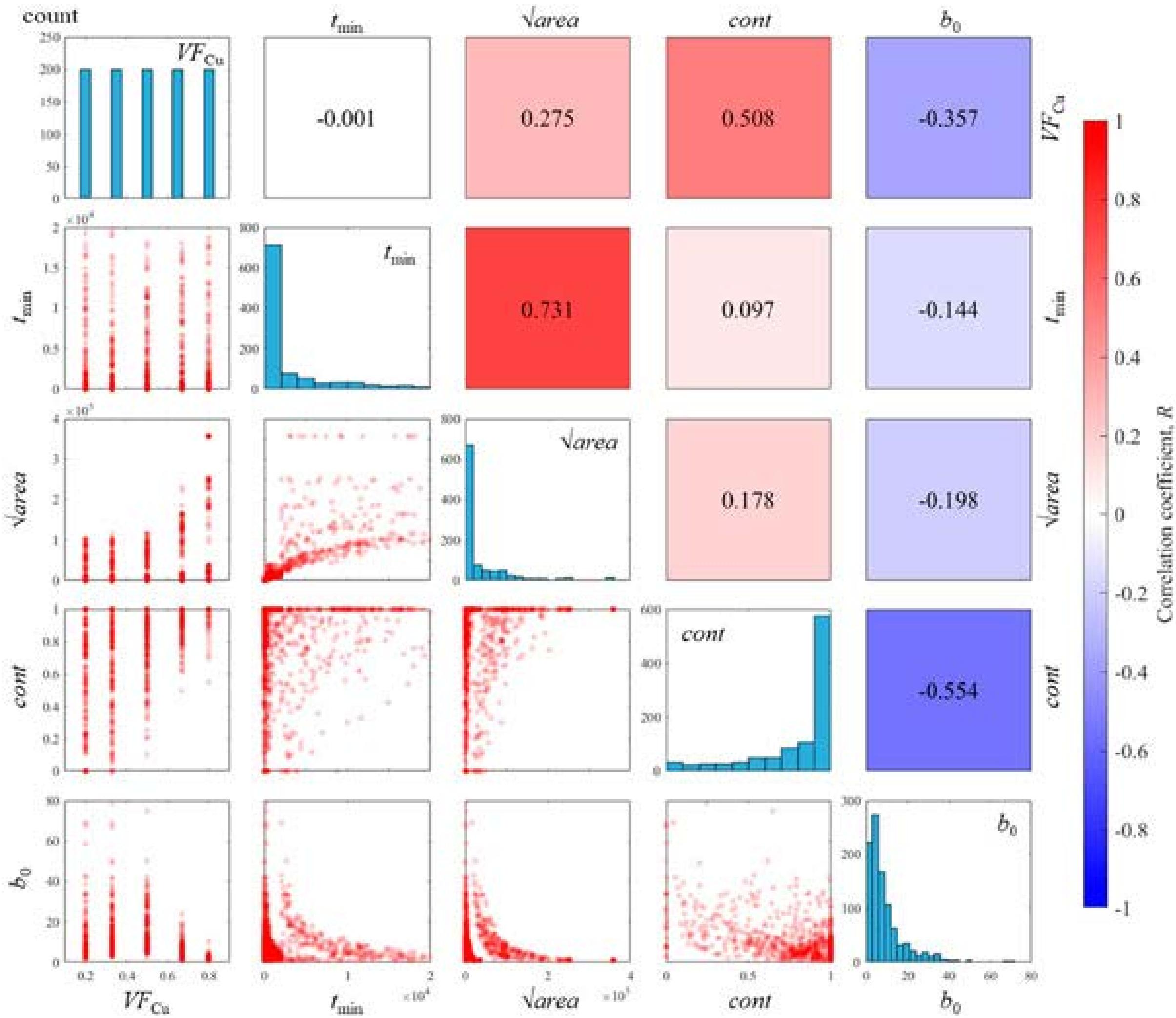

Fig. 10

Correlation analysis of microstructural descriptors of high importance. The diagonal component is a histogram of each descriptor, the lower left elements are scatter plots between two descriptors, and the upper right elements are the correlation coefficients between two descriptors.

4. Discussion

4.1 Significant microstructure descriptors for strength and conductivity

The importance analysis with RF regression revealed that the volume fraction (VF_{Cu}) is significant on both yield stress and electrical conductivity. Increasing the VF_{Cu} leads to a decrease in yield stress and an increase in conductivity. Conversely, decreasing VF_{Cu} results in the opposite effect. Therefore, VF_{Cu} cannot serve as a descriptor for overcoming the trade-off between these properties. The layer thickness (t_{min}) was also found to be crucial for both yield stress and conductivity. Similar to VF_{Cu}, varying layer thickness creates a trade-off between these two properties. However, as depicted in Fig. 8(b), the decrease in conductivity due to layer thickness is modest. In contrast, the yield stress improves by approximately threefold. Therefore, reducing layer thickness can be a viable approach to improve the strength of Cu/Nb laminates.

Apart from volume fraction and layer thickness, the 0th Betti number for yield stress and layer continuity for electrical conductivity were identified as key descriptors. The relationship between yield stress and the 0th Betti number is illustrated in Fig. 11(a). To clarify the trend, only the results of phase maps with the same RVE size were plotted. The figure shows that the yield stress increases with the

0th Betti number. The 0th Betti number corresponds to the number of Cu objects within the RVE. A higher value indicates a more finely separated Cu phase and a larger proportion of Nb phase. Thus, the 0th Betti number includes the effects of both volume fraction and layer thickness. This is not apparent from the correlation coefficients in Fig. 10, because as their relationship is nonlinear. In addition, the separation of Cu layers along the *x*-axis direction, which cannot be evaluated by layer thickness, is also counted in the 0th Betti number. This is probably the reason why the Betti number was considered more important than layer thickness in the RF analysis. Previous studies in dual-phase (DP) steels also suggested that the 0th Betti number could be an effective descriptor in addressing the trade-off problem between strength and ductility [26]. It has been reported that the Betti number is also effective in evaluating the stiffness of two-phase materials [36] and the elastic energy of polycrystalline materials [37]. The Betti number may be an essential descriptor in evaluating the mechanical properties of two-phase materials. When examining the importance of other descriptors on yield stress, in contrast to the results for conductivity, layer continuity was less important compared to other geometric descriptors such as curvature, perimeter, and circularity. This suggests that in elastoplastic deformation, stress concentration behaviors due to local shapes are more critical than the long-range connectivity of the entire model. The importance of covariograms (*BI* and *HM*) and spatial correlation (*SC*) was moderate. One of the limitations of the current research is the relatively small RVE size resulting from iterative computations. These importances may change by changing the RVE size. The persistent homology (PH) also exhibits RVE size dependence. Although there are no clear reports on the number of points in PD required for machine learning, many studies have used PDs containing between 100 to 1000 points [38, 39]. In the current study, the maximum number of points on the PD was 79 due to RVE size limitations. The importance of *PH* may change if the RVE size is increased. Comparing *SC* and *PH* in Fig. 9(a), *SC* was relatively more important. This also suggests that stress concentration caused by local structures and the resulting stress concentration are more dominant in macroscopic mechanical properties than the connectivity of the phase.

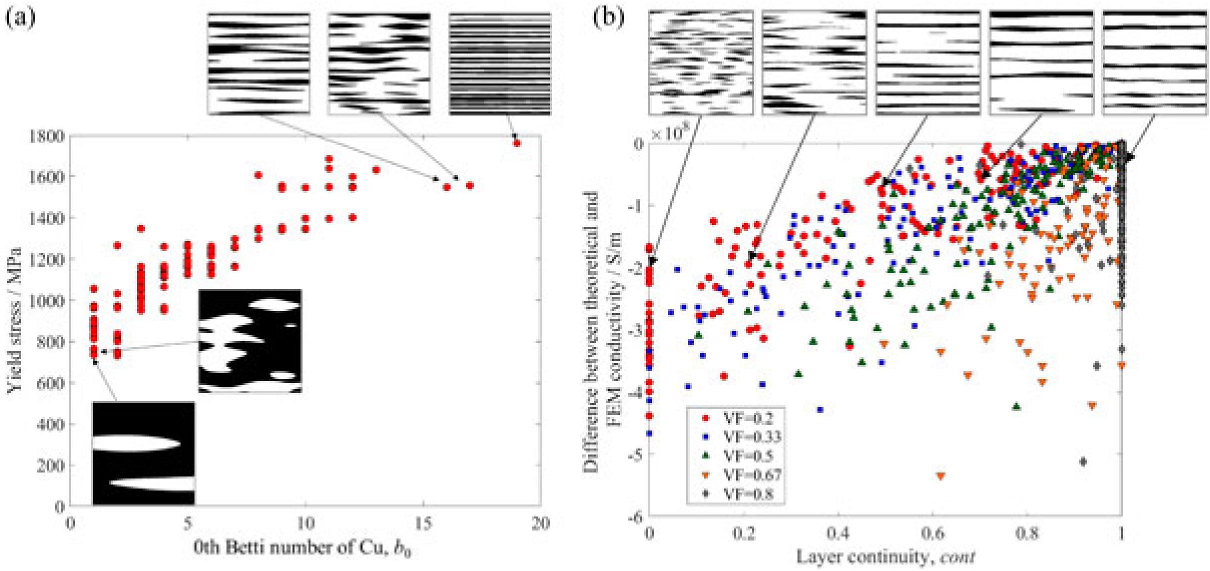

Fig. 11

(a) Effect of 0th Betti number on yield stress when RVE size is 200 nm and (b) effect of layer continuity on conductivity.

To analyze the relationship between electrical conductivity and layer continuity, Fig. 11(b) presents a plot of the difference between the theoretical value of conductivity for parallel circuits (eq. (8)) and the conductivity calculated from FEM against layer continuity. The higher VF_{Cu} increases the chance of Cu layers connecting, resulting in higher layer continuity. This trend is also evident from the positive correlation between VF_{Cu} and *cont* shown in Fig. 10. In all cases of Cu volume fraction, it was found that the conductivity approaches the theoretical value as the layer connectivity increases. Contrary to percolation theory [40], where the conductivity of a mixture of conductors and insulators increases rapidly upon exceeding a certain threshold, the conductivity of Cu/Nb laminate changed continuously and smoothly with connectivity, including cases where layer continuity was zero, i.e., no continuous Cu layers. This is because both phases are conductive materials and current flows through the Nb phase even when the Cu layer is not connected. The significant scattering in the figure can be attributed to the fact that layer continuity alone does not account for the variation of layer thickness and branching. PH is known to be an effective tool for assessing connectivity, but it has the disadvantage of not being able to account for anisotropy. Since connectivity in the current loading direction contributes to macroscopic conductivity, layer continuity, which selectively extracts connectivity in the *x*-direction, has become more important than *PH*. The *SC* extracts directional information but primarily focuses on the relative positioning between two nearby points. It may not effectively capture long-range connectivity across the left and right edges of the RVE. As shown in Fig. 9(b), SC_2 exhibited a moderate importance. The SC_2 potentially captures the relative positioning between two nearby points, including layer thickness variation and branching, suggesting that combining *cont* and SC_2 may enable more accurate predictions of conductivity.

4.2 Pareto front in the trade-off between strength and conductivity

As mentioned in the introduction, developing higher-performance materials necessitates solving multi-objective optimization in the structure-properties linkages. Multi-objective optimization is the problem of simultaneously maximizing multiple objective functions, each of which usually competes with the other, making it difficult to optimize all objectives simultaneously. In such multi-objective optimization problems, Pareto optimum refers to a situation in which at least one objective cannot be improved without compromising the other objectives. The Pareto front represents a set of these Pareto optimal solutions and represents the ideal trade-off boundary. In complex decision problems with multiple objectives, such as materials design, this Pareto front supports the most balanced decision. Based on the yield stress and conductivity obtained in FEA, Pareto fronts in yield stress-conductive space are plotted in Fig. 12(a). The Pareto front on the high conductivity side consisted of data points with high Cu volume fraction, while the front on the high strength side consisted of data points with small layer thickness. It was also found that the Pareto front could not be expanded when the Cu volume fraction was less than 0.50. Indeed, the Cu volume fractions of Cu/Nb laminates reported to date typically range between 0.5 and 0.67. As discussed in the previous section, layer connectivity and the 0th Betti number play a crucial role in enhancing yield strength and electrical conductivity, respectively. To increase the 0th Betti number, it is necessary to augment the number of connected Cu layers, while improving layer connectivity corresponds to controlling the phase interfaces to prevent discontinuities in the Cu layers. Consequently, one of ideal phase maps would feature completely smooth interfaces with minimal layer thickness. To verify this, phase maps with a layer thickness of 5 nm and perfectly flat interfaces were manually created (Fig. 12(b)), and FEA was performed to calculate the yield stress and conductivity. For comparison, calculations were also conducted for ideal phase maps with a layer thickness of 20 μm. The results are plotted in Fig. 12(a). As evident from the figure, these ideal phase maps form a Pareto front. This indicates that manufacturing processes capable of creating fine microstructures with preserved connections of each Cu layer are indispensable for overcoming trade-offs.

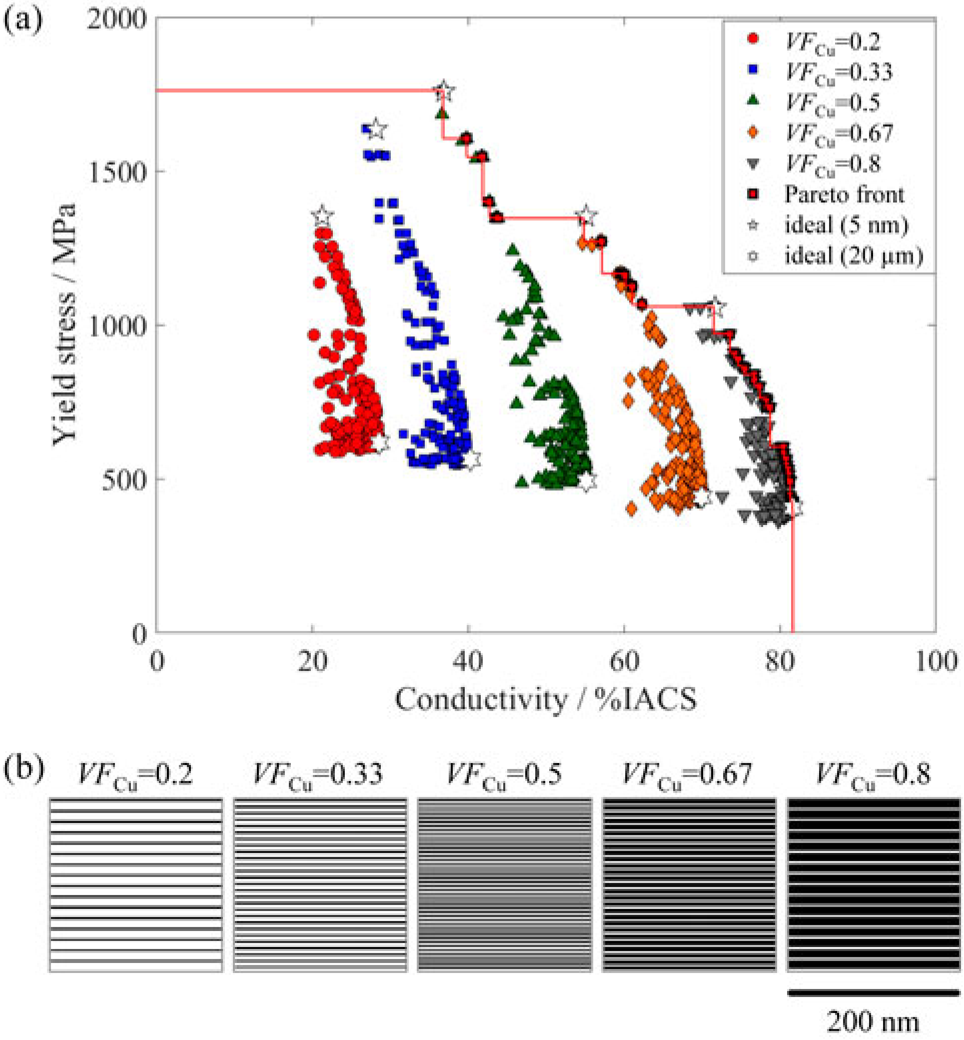

Fig. 12

(a) Pareto front in yield stress-conductive space and (b) ideal phase maps with layer thickness of 5 nm.

Although the Pareto front was considered here within a 2D space of strength and conductivity, a similar approach could be used to define a Pareto solution in a multidimensional space with forward analysis of other properties such as ductility and fatigue strength. To assess the maximum tensile strength and elongation to failure, it is necessary to understand the strain partitioning in the hard and soft phases and the evolution of voids [41], which requires the introduction of a damage law. The current research varied only the spatial distribution of the two phases, without considering the crystal grain geometries and crystallographic orientation. It is well known that finer grain size increases strength [42–45]. Experimental reports indicate that crystalline texture affect mechanical strength, resulting in anisotropy in static strength and fatigue life [9, 13]. There is also anisotropy in the interface irregularities formed by the rolling process. In cases of anisotropy in grain shape, employing crystal plasticity finite element analysis with the Kocks-Mecking law, adapted to account for dislocation accumulation at grain boundaries, might adeptly address Hall-Petch behavior [46]. Furthermore, recent work by Blaschke *et al.* on the electrical conductivity of Cu/Nb composites revealed the importance of grain size effects, especially when layer thickness is considerable [47]. They have proposed a model for predicting conductivity that takes into account the effects of grain boundaries. A more accurate prediction of electrical conductivity can be achieved by considering scattering by grain boundaries and dislocations [14]. Therefore, by conducting FEA taking into account crystal plasticity and electron scattering due to grain boundaries and dislocations, it may be possible to further expand the Pareto front through the optimization of microstructures and processes in the future.

5. Conclusions

Simple FEA was performed on Cu/Nb two-phase laminates, and MI approaches were applied to analyze the relationship between microstructural descriptors and electrical/mechanical properties. The following conclusions were drawn:

1. (1) The two-phase structure of the ARB Cu/Nb laminate could be approximately reconstructed by representing the interface geometry as a sinusoidal wave containing random numbers. The yield stress was accurately reproduced by applying the Hall-Petch type empirical equation for layer thickness to the FEA. Additionally, conductivity was successfully reproduced using empirical formulas for phonon and interface scattering.
2. (2) By varying layer thickness and the morphology of the two phases and performing numerous calculations, a database linking microstructural descriptors with mechanical and electrical properties was created. Importance analysis using random forest regression indicated that the Cu volume fraction, layer thickness, and the 0th Betti number were particularly important for yield stress. Local geometric descriptors such as curvature, perimeter, circularity, and spatial correlation functions were also relatively important.
3. (3) For electrical conductivity, the Cu volume fraction had the strongest influence, followed by layer thickness and layer continuity. Features describing long-distance connectivity were more crucial than local geometric descriptors.
4. (4) Based on the yield stress and conductivity obtained from the FEA, the Pareto front in the trade-off between strength and conductivity of ARB Cu/Nb laminates was presented. To develop higher-performance Cu/Nb laminates, it was shown that maintaining a Cu volume fraction above 0.5, keeping layer thickness small, and improving layer continuity is necessary.

Acknowledgments

This work was partially supported by JSPS KAKENHI Grant Numbers 23H04464 and JST SICORP Grant Number JPMJSC21E1, Japan. MJ acknowledges support from A*STAR, Singapore via the Structural Metals and Alloys Programme (Grant No. A18B1b0061).

REFERENCES

- 1) L. Lu, Y. Shen, X. Chen, L. Qian and K. Lu: Ultrahigh Strength and High Electrical Conductivity in Copper, Science **304** (2004) 422–426. doi:10.1126/science.1092905
- 2) M. Kaltenbrunner, T. Sekitani, J. Reeder, T. Yokota, K. Kuribara, T. Tokuhara, M. Drack, R. Schwödiauer, I. Graz, S. Bauer-Gogonea, S. Bauer and T. Someya: An ultra-lightweight design for imperceptible plastic electronics, Nature **499** (2013) 458–463. doi:10.1038/nature12314
- 3) M. Koo, K.-I. Park, S.H. Lee, M. Suh, D.Y. Jeon, J.W. Choi, K. Kang and K.J. Lee: Bendable Inorganic Thin-Film Battery for Fully Flexible Electronic Systems, Nano Lett. **12** (2012) 4810–4816. doi:10.1021/nl302254v
- 4) S. Kim, C. Laschi and B. Trimmer: Soft robotics: a bioinspired evolution in robotics,

Trends Biotechnol. **31** (2013) 287–294. doi:10.1016/j.tibtech.2013.03.002

- 5) I.J. Beyerlein, N.A. Mara, J. Wang, J.S. Carpenter, S.J. Zheng, W.Z. Han, R.F. Zhang, K. Kang, T. Nizolek and T.M. Pollock: Structure–Property–Functionality of Bimetal Interfaces, JOM **64** (2012) 1192–1207. doi:10.1007/s11837-012-0431-0
- 6) T. Nizolek, N.A. Mara, I.J. Beyerlein, J.T. Avallone, J.E. Scott and T.M. Pollock: Processing and Deformation Behavior of Bulk Cu–Nb Nanolaminates, Metallogr. Microstruct. Anal. **3** (2014) 470–476. doi:10.1007/s13632-014-0172-2
- 7) C. Ding, J. Xu, D. Shan, B. Guo and T.G. Langdon: Sustainable fabrication of Cu/Nb composites with continuous laminated structure to achieve ultrahigh strength and excellent electrical conductivity, Compos. Part B **211** (2021) 108662. doi:10.1016/j.compositesb.2021.108662
- 8) T. Nizolek, I.J. Beyerlein, N.A. Mara, J.T. Avallone and T.M. Pollock: Tensile behavior and flow stress anisotropy of accumulative roll bonded Cu-Nb nanolaminates, Appl. Phys. Lett. **108** (2016) 051903. doi:10.1063/1.4941043
- 9) Y. Zhang, J.G. Gigax, T.J. Nizolek, J.S. Carpenter, M.M. Schneider, N. Li, L. Capolungo and R.J. McCabe: Tensile and failure behaviors of Cu/Nb nanolaminates: the effects of loading direction, layer thickness, and annealing, Acta Mater. **240** (2022) 118346. doi:10.1016/j.actamat.2022.118346
- 10) A. Misra, J.P. Hirth and R.G. Hoagland: Length-scale-dependent deformation mechanisms in incoherent metallic multilayered composites, Acta Mater. **53** (2005) 4817–4824. doi:10.1016/j.actamat.2005.06.025
- 11) A.S. Budiman, R. Sahay, H.P. Anwar Ali, S.K. Tippabhotla, I. Radchenko and N. Raghavan: Interface-mediated plasticity and fracture in nanoscale Cu/Nb multilayers as revealed by *in situ* clamped microbeam bending, Mater. Sci. Eng. A **803** (2021) 140705. doi:10.1016/j.msea.2020.140705
- 12) Y. Chen, N. Li, R.G. Hoagland, X.Y. Liu, J.K. Baldwin, I.J. Beyerlein, J.Y. Cheng and N.A. Mara: Effects of three-dimensional Cu/Nb interfaces on strengthening and shear banding in nanoscale metallic multilayers, Acta Mater. **199** (2020) 593–601. doi:10.1016/j.actamat.2020.08.019
- 13) F. Briffod, K. Yasuda, T. Shiraiwa, M.H. Jhon, F. Gunawan, A.S. Budiman and M. Enoki: Effect of Microstructure on the Tensile and Fatigue Behavior of an Accumulative Roll Bonded Cu/Nb Laminate Material, Mater. Trans. **65** (2024) 167–176. doi:10.2320/matertrans.MT-M2023081
- 14) D.N. Blaschke, C. Miller, R. Mier, C. Osborn, S.M. Thomas, E.L. Tegtmeier, W.P. Winter, J.S. Carpenter and A. Hunter: Predicting electrical conductivity in Cu/Nb composites: A combined model-experiment study, J. Appl. Phys. **132** (2022) 045105. doi:10.1063/5.0096880
- 15) K. Nakashima, T. Kunimine, R. Monzen, N. Muramatsu and S. Ueno: Effect of Microstructure on Strength and Electrical Conductivity of Cu–3.8 wt%Zr Alloy Wires, Mater. Trans. **65** (2024) 130–137. doi:10.2320/matertrans.MT-D2023007
- 16) J.E. González-Hernández and J.M. Cubero-Sesin: Electrical Conductivity of Ultrafine-Grained Cu and Al Alloys: Attaining the Best Compromise with Mechanical Properties, Mater. Trans. **64** (2023) 1754–1768. doi:10.2320/matertrans.MT-MF2022046
- 17) S.W.C.P.C.P. Ghosh: *Integrated Computational Materials Engineering (ICME): Advancing*

Computational and Experimental Methods, (Springer, NY, 2020).

- 18) M. Demura: Materials Integration for Accelerating Research and Development of Structural Materials, Mater. Trans. **62** (2021) 1669–1672. doi:10.2320/matertrans.MT-M2021135
- 19) J.S. Carpenter, R.J. McCabe, S.J. Zheng, T.A. Wynn, N.A. Mara and I.J. Beyerlein: Processing Parameter Influence on Texture and Microstructural Evolution in Cu-Nb Multilayer Composites Fabricated *via* Accumulative Roll Bonding, Metall. Mater. Trans. A **45** (2014) 2192–2208. doi:10.1007/s11661-013-2162-4
- 20) G. Matheron: *Éléments pour une Théorie des Milieux Poreux*, (Masson et Cie, Paris, 1967).
- 21) B. Krebs, A. Hazotte, L. Germain and M. Gouné: QUANTITATIVE ANALYSIS OF BANDED STRUCTURES IN DUAL-PHASE STEELS, Image Anal. Stereol. **29** (2010) 85–90. doi:10.5566/ias.v29.p85-90
- 22) S. Torquato: *Random Heterogeneous Materials*, (Springer-Verlag, New York, 2002).
- 23) D.T. Fullwood, S.R. Niezgoda and S.R. Kalidindi: Microstructure reconstructions from 2-point statistics using phase-recovery algorithms, Acta Mater. **56** (2008) 942–948. doi:10.1016/j.actamat.2007.10.044
- 24) Y. Hiraoka, T. Nakamura, A. Hirata, E.G. Escolar, K. Matsue and Y. Nishiura: Hierarchical structures of amorphous solids characterized by persistent homology, Proc. Natl. Acad. Sci. USA **113** (2016) 7035–7040. doi:10.1073/pnas.1520877113
- 25) I. Obayashi, Y. Hiraoka and M. Kimura: Persistence diagrams with linear machine learning models, Journal of Applied and Computational Topology **1** (2018) 421–449. doi:10.1007/s41468-018-0013-5
- 26) T. Shiraiwa, S. Kato, F. Briffod and M. Enoki: Exploration of outliers in strength–ductility relationship of dual-phase steels, Science and Technology of Advanced Materials: Methods **2** (2022) 175–197. doi:10.1080/27660400.2022.2080483
- 27) T. Shiraiwa, F. Briffod, M. Enoki and K. Yamazaki: Inverse analysis of the relationship between three-dimensional microstructures and tensile properties of dual-phase steels, Mater. Today Commun. **33** (2022) 104958. doi:10.1016/j.mtcomm.2022.104958
- 28) N. Li, J. Wang, A. Misra and J.Y. Huang: Direct Observations of Confined Layer Slip in Cu/Nb Multilayers, Microsc. Microanal. **18** (2012) 1155–1162. doi:10.1017/S143192761200133X
- 29) S. Subedi, I.J. Beyerlein, R. LeSar and A.D. Rollett: Strength of nanoscale metallic multilayers, Scr. Mater. **145** (2018) 132–136. doi:10.1016/j.scriptamat.2017.04.009
- 30) L. Tian, I. Anderson, T. Riedemann and A. Russell: Modeling the electrical resistivity of deformation processed metal–metal composites, Acta Mater. **77** (2014) 151–161. doi:10.1016/j.actamat.2014.06.013
- 31) J.D. Verhoeven, H.L. Downing, L.S. Chumbley and E.D. Gibson: The resistivity and microstructure of heavily drawn Cu-Nb alloys, J. Appl. Phys. **65** (1989) 1293–1301. doi:10.1063/1.343024
- 32) G. Scocchi, A. Ortona, L. Grossi, G. Bianchi, C. D'Angelo, T. Leidi and R. Gilardi: Evaluation of a simple finite element method for the calculation of effective electrical conductivity of compression moulded polymer–graphite composites, Compos. Part A **48** (2013) 15–25. doi:10.1016/j.compositesa.2012.12.013
- 33) E. Chang, A. Ameli, A.R. Alian, L.H. Mark, K. Yu, S. Wang and C.B. Park:

Percolation mechanism and effective conductivity of mechanically deformed 3-dimensional composite networks: Computational modeling and experimental verification, Compos. Part B **207** (2021) 108552. doi:10.1016/j.compositesb.2020.108552

- 34) W.Y. Loh: REGRESSION TRESS WITH UNBIASED VARIABLE SELECTION AND INTERACTION DETECTION, Stat. Sin. **12** (2002) 361–386.
- 35) R. Genuer, J.-M. Poggi and C. Tuleau-Malot: Variable selection using random forests, Pattern Recognit. Lett. **31** (2010) 2225–2236. doi:10.1016/j.patrec.2010.03.014
- 36) D.D. Gerrard, D.T. Fullwood, D.M. Halverson and S.R. Niezgoda: Computational Homology, Connectedness, and Structure-Property Relations, Computers, Materials & Continua **15** (2010) 129–152. doi:10.3970/cmc.2010.015.129
- 37) T. Wanner, E.R. Fuller, Jr. and D.M. Saylor: Homology metrics for microstructure response fields in polycrystals, Acta Mater. **58** (2010) 102–110. doi:10.1016/j.actamat.2009.08.061
- 38) Y. Skaf and R. Laubenbacher: Topological data analysis in biomedicine: A review, J. Biomed. Inform. **130** (2022) 104082. doi:10.1016/j.jbi.2022.104082
- 39) C.S. Pun, S.X. Lee and K. Xia: Persistent-homology-based machine learning: a survey and a comparative study, Artif. Intell. Rev. **55** (2022) 5169–5213. doi:10.1007/s10462-022-10146-z
- 40) V.K.S. Shante and S. Kirkpatrick: An introduction to percolation theory, Adv. Phys. **20** (1971) 325–357. doi:10.1080/00018737100101261
- 41) R. Kato, N. Koga and C. Watanabe: Strength-Electrical Conductivity Balances of Cu/Martensite Steel Multilayered Sheets with Various Volume Ratios, Mater. Trans. **65** (2024) 205–211. doi:10.2320/matertrans.MT-M2023145
- 42) M. Liu, B.B. Wang, X.H. An, P. Xue, F.C. Liu, L.H. Wu, D.R. Ni, B.L. Xiao and Z.Y. Ma: Friction stir additive manufacturing enabling scale-up of ultrafine-grained pure copper with superior mechanical properties, Mater. Sci. Eng. A **857** (2022) 144088. doi:10.1016/j.msea.2022.144088
- 43) S.A. Hosseini and H.D. Manesh: High-strength, high-conductivity ultra-fine grains commercial pure copper produced by ARB process, Mater. Des. **30** (2009) 2911–2918. doi:10.1016/j.matdes.2009.01.012
- 44) R. Floriano and K. Edalati: Effects of Severe Plastic Deformation on Advanced Biomaterials for Biomedical Applications: A Brief Overview, Mater. Trans. **64** (2023) 1673–1682. doi:10.2320/matertrans.MT-MF2022043
- 45) M.Y. Murashkin, N.A. Enikeev and X. Sauvage: Potency of Severe Plastic Deformation Processes for Optimizing Combinations of Strength and Electrical Conductivity of Lightweight Al-Based Conductor Alloys, Mater. Trans. **64** (2023) 1833–1843. doi:10.2320/matertrans.MT-MF2022048
- 46) S. Haouala, R. Alizadeh, T.R. Bieler, J. Segurado and J. Llorca: Effect of slip transmission at grain boundaries in Al bicrystals, Int. J. Plast. **126** (2020) 102600. doi:10.1016/j.ijplas.2019.09.006
- 47) D.N. Blaschke, C. Miller, R. Mier, C. Osborn, S.M. Thomas, E.L. Tegtmeier, W.P. Winter, J.S. Carpenter and A. Hunter: Predicting electrical conductivity in Cu/Nb composites: A combined model-experiment study, J. Appl. Phys. **132** (2022) 045105. doi:10.1063/5.0096880